Title

Resolving Surface Rain from GMI High-Frequency Channels: Limits Imposed by the Three-Dimensional Structure of Precipitation Resolving Surface Rain from GMI High-Frequency Channels: Limits Imposed by the Three-Dimensional Structure of Precipitation

Journal

Journal of Atmospheric and Oceanic Technology, 35(9)

ISSN

0739-0572

Authors

Guilloteau, Clément
Foufoula-Georgiou, Efi
Kummerow, Christian D
et al.

Publication Date

2018-09-01

DOI

10.1175/jtech-d-18-0011.1

Peer reviewed

Resolving Surface Rain from GMI High-Frequency Channels: Limits Imposed by the Three-Dimensional Structure of Precipitation

CLÉMENT GUILLOTEAU AND EFI FOUFOULA-GEORGIOU

Department of Civil and Environmental Engineering, University of California, Irvine, Irvine, California

CHRISTIAN D. KUMMEROW AND VELJKO PETKOVIĆ

Department of Atmospheric Science, Colorado State University, Fort Collins, Colorado

(Manuscript received 6 February 2018, in final form 15 June 2018)

ABSTRACT

The scattering of microwaves at frequencies between 50 and 200 GHz by ice particles in the atmosphere is an essential element in the retrieval of instantaneous surface precipitation from spaceborne passive radiometers. This paper explores how the variable distribution of solid and liquid hydrometeors in the atmospheric column over land surfaces affects the brightness temperature (TB) measured by GMI at 89 GHz through the analysis of Dual-Frequency Precipitation Radar (DPR) reflectivity profiles along the 89-GHz beam. The objective is to refine the statistical relations between observed TBs and surface precipitation over land and to define their limits. As GMI is scanning with a 53° Earth incident angle, the observed atmospheric volume is actually not a vertical column, which may lead to very heterogeneous and seemingly inconsistent distributions of the hydrometeors inside the beam. It is found that the 89-GHz TB is mostly sensitive to the presence of ice hydrometeors several kilometers above the 0°C isotherm, up to 10 km above the 0°C isotherm for the deepest convective systems, but is a modest predictor of the surface precipitation rate. To perform a precise mapping of atmospheric ice, the altitude of the individual ice clusters must be known. Indeed, if variations in the altitude of ice are not accounted for, then the high incident angle of GMI causes a horizontal shift (parallax shift) between the estimated position of the ice clusters and their actual position. We show here that the altitude of ice clusters can be derived from the 89-GHz TB itself, allowing for correction of the parallax shift.

1. Introduction

Launched in 2014, the Global Precipitation Measurement (GPM; acronyms are also defined in the appendix) *Core Observatory* carries the passive GPM Microwave Imager (GMI) along with a Dual-Frequency Precipitation Radar (DPR). Both instruments are dedicated to the observation of clouds and precipitation processes (Hou et al. 2014; Skofronick-Jackson et al. 2016). The 13 channels of GMI measure vertically and horizontally polarized radiances between 10.6 and 183 GHz. The measured radiances are the product of the interaction of surface-emitted radiation with water vapor, liquid, and solid hydrometeors in the atmosphere. The radiances are converted into brightness temperatures (TBs) for physical interpretation. The 183-GHz channels are primarily sensitive to water vapor absorption and ice scattering. While channels between 80 and 170 GHz are also most sensitive to ice scattering, channels between 10 and 40 GHz are most sensitive to emission by liquid raindrops (and by water vapor for the 23-GHz channel). The DPR emits short pulses at 13.6 GHz (Ku band) and 35.5 GHz (Ka band) and measures the echoes from hydrometeors. While the DPR can resolve the three-dimensional structure of precipitation systems, GMI offers a much wider swath width (885 km compared to the 245-km swath of the DPR). Moreover, while the DPR is the only scanning precipitation radar currently in orbit, a number of passive microwave imagers similar to GMI are orbiting Earth on board various satellites. Among them are SSM/IS on board the DMSP satellite

Denotes content that is immediately available upon publication as open access.

Corresponding author: Clément Guilloteau, cguillot@uci.edu

DOI: 10.1175/JTECH-D-18-0011.1

series and AMSR-2 on board *Global Change Observation Mission–Water* (*GCOM-W1*). Because of this, at a given point of the globe, passive microwave observations are available much more frequently than the radar measurements. Having a radar and a passive imager on board the same satellite not only allows for improved retrievals utilizing both sensors (Grecu et al. 2016) but also the generation of a large quantity of collocated passive microwave observations and 3D radar reflectivity profiles that can be used to define parametric empirical or physical relations between precipitation rates and microwave brightness temperatures.

Various operational algorithms for the retrieval of surface precipitation from passive microwave such as NASA's GPROF (Kummerow et al. 2001, 2015), JAXA's GSMaP (Aonashi et al. 2009), and the Satellite Application Facility on Support to Operational Hydrology and Water Management (H SAF)'s Cloud Dynamics and Radiation Database (H 01-CDRD; Mugnai et al. 2013), as well as experimental algorithms (Petty and Li 2013; Ebtehaj et al. 2015), have been designed relying on GPM data and on data from its predecessor, TRMM (Kummerow et al. 1998, 2000). The GPROF algorithm for GMI performs a dictionary-based Bayesian inversion of the 13 observed TBs to retrieve near-surface precipitation. For each vector of observed TBs, the algorithm searches for similar vectors in an a priori database (dictionary). The final GPROF estimate is a Bayesian weighted average of the precipitation rates associated with each of the retained dictionary vectors. The dictionary consists of a large number (several million) of observed DPR reflectivity profiles and associated microwave TBs simulated by a physical radiative transfer model. In practice, 14 different dictionaries are used over oceans and over different types of land surface. Because the observed vector of microwave TBs depends on the density, size distribution, and radiometric properties of solid and liquid hydrometeors along the atmospheric column at every altitude level, the surface precipitation cannot be rigorously retrieved without accounting for the rest of the atmospheric column. The number of necessary parameters to comprehensively describe any atmospheric hydrometeor profile (ideally, the density and size distribution of each possible type of hydrometeor specified at every altitude level) is always greater than the dimension of the vector of observed TBs. The inversion problem is therefore dramatically underdetermined, leading to an inherent retrieval uncertainty.

Several evaluation studies of passive microwave retrievals have revealed heterogeneous performances depending on geographical areas, seasons, and types of precipitation systems (Tang et al. 2014; Oliveira et al. 2015; Liu et al. 2017; Petković and Kummerow 2017; Guilloteau et al. 2017). The passive microwave retrieval over oceans generally outperforms the retrieval over land. In Guilloteau et al. (2017), the joint spatial variations of DPR and GPROF surface precipitation fields were analyzed through a wavelet-based multiscale decomposition. It was demonstrated that the GMI retrieval of surface precipitation with the GPROF algorithm hardly resolves scales finer than 40 km over land; that is, below the 40-km scale, the spatial variations in GMI GPROF fields are not consistent with the DPR. At the same time, GMI GPROF was found able to resolve scales down to 10–20 km over oceans. This is partially explained by the fact that the high and variable emissivity of land surfaces makes the interpretation of low-frequency TBs (below 40 GHz) ambiguous, as the precipitation and the surface have similar emitting temperatures; while over oceans, variations in the low-frequency TBs can be relatively easily interpreted as an emission signal from rain. Therefore, the retrieval over land mostly relies on high frequencies, which are sensitive to cloud ice content, as the scattering of microwaves by ice particles leads to depression in the observed TBs above 40 GHz. In fact, the early-developed algorithms used only TBs at frequencies higher than 80 GHz for the retrieval over land (Gopalan et al. 2010); this was the case in particular for the TRMM-era versions of the GPROF algorithm.

This paper presents a joint statistical analysis of GMI TBs at 89 GHz and DPR reflectivities over the southeastern continental United States. The objective is to evaluate how the three-dimensional structure of clouds and precipitation systems affects observed TBs at 89 GHz. In particular, we evaluate and quantify the effect of the 52.8° Earth incidence angle of GMI and the resulting parallax shift on observed TBs from the perspective of the retrieval of surface precipitation. The evaluation is performed by analyzing three-dimensional reflectivity profiles from the DPR within and around GMI's 89 GHz field of view. The objective is to determine to what extend the 89-GHz brightness temperature observed by a conical-scan imager is related first to the cloud ice content and second to surface precipitation, for various types of precipitation systems. Finally, we show that simple assumptions on the altitude of the ice to which the 89-GHz TB is responding can be used to adjust for the parallax shift effect and to improve the empirical relationship between TB and surface precipitation. The paper is organized as follows: The dataset used for the study are presented in section 2. Section 3 presents the analysis of collocated GMI TBs and DPR reflectivity profiles, and the last section discusses the results and presents the conclusions.

2. Data

a. GMI 89-GHz vertically polarized brightness temperature

The passive microwave imager GMI on board the GPM *Core Observatory* conically scans the atmosphere below the satellite at a scanning angle of 48.5°, which, considering the Earth's curvature and the altitude of the satellite, leads to a 52.8° Earth incident angle. While GMI has 13 channels [see Draper et al. (2015) for a detailed description], in this article, we consider only the 89-GHz vertically polarized channel (89V) to provide a simple univariate analysis. GMI brightness temperatures are distributed by NASA under the GPM_1CGMI_V05 product (GPM Science Team 2016a). The −3-dB footprint of the 89V channel at surface level is an ellipse with minor and major axes of 4.4 and 7.1 km, respectively. Each scan, made of 221 individual beam positions (i.e., pixels), covers an 885-km-wide swath at Earth's surface. The distance between two successive scans along the satellite's displacement direction is 13.5 km. Within a scan, two adjacent pixels are 5 km apart.

b. KuPR reflectivity profiles

The Dual-Frequency Precipitation radar on board the GPM *Core Observatory* is made of two radars: the Ku precipitation radar (KuPR) operating at 13.6 GHz and the Ka precipitation radar (KaPR) operating at 35.5 GHz. Both radars have a 5-km nominal horizontal resolution at the surface, with a 250-m vertical resolution (176 overlapping bins between surface level and 22-km altitude). Here, only the KuPR reflectivity profiles are considered. The KuPR is a more mature technology than its Ka-band counterpart, thanks to the 17 years of operation of a similar radar on board TRMM between 1997 and 2015 (Kummerow et al. 1998; Houze et al. 2015). Moreover, the KuPR swath, embedded in the GMI swath, is 245 km (while the KaPR swath is only 120 km), allowing collocation with GMI over a larger area. While the minimum detectable reflectivity of the KuPR is 12 dBZ, reflectivities below 14 dBZ are considered as "no echo" in this article. In contrast to GMI, the KuPR has a cross-track scan, with a scanning angle varying within ±17°. In this study, attenuation-corrected reflectivities from the GPM_2AKu_V05 product (GPM Science Team 2016b) are used.

c. 2-m temperature and altitude of the 0°C isotherm

Two ancillary datasets are used for this analysis. The 2-m temperature T_{2m} from the ECMWF interim reanalysis (ERA-Interim) is used as a proxy for the surface temperature. This 2-m temperature is also used as a priori information by the GPROF retrieval algorithm over land (Petković et al. 2018). The collocation of T_{2m} with GMI observations is performed by the NASA GPM Science Team. In the present study, all the KuPR profiles are aligned on the 0°C (273.15 K) isotherm for comparison and averaging. For each KuPR profile, the 0°C isotherm is provided by the Japan Meteorological Agency Global Analysis (GANAL) (Awaka et al. 2016). The 0°C isotherm is included in the GPM_2AKu_V05 product files.

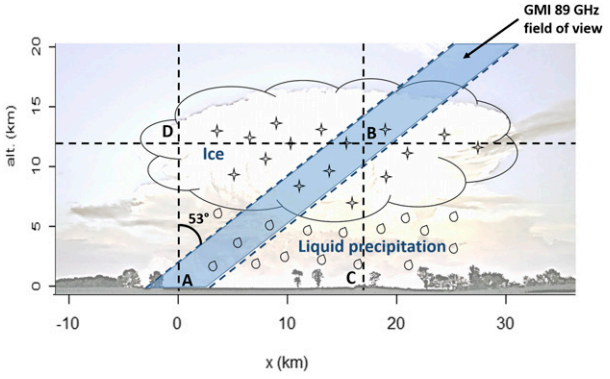

FIG. 1. Schematic representation of the vertical cross section of GMI's 89-GHz field of view in the atmosphere. Point A is the intersection of the beam with the surface. Point B is the center of gravity of the ice inside the beam. Point C is the vertical projection of point B on the surface. For the collocation with KuPR reflectivity profiles, along-beam profiles are constructed along the AB axis.

3. Joint Analysis of GMI and KuPR observations

a. Approach

As stated before, the footprint at the surface of GMI's 89-GHz beam is a 4.4 km × 7.1 km ellipse. Considering the pointing accuracy of GMI (Draper et al. 2015), the position of the intersection of each beam with Earth's surface is known with a precision of a few hundred meters. Nevertheless, because GMI is a passive imager, it cannot resolve the height from which the signal is emanating. Because of the 53° incidence angle, the uncertainty on the height also induces an uncertainty on the horizontal position. Therefore, the exact position of the hydrometeors eventually affecting the observed TB in both the vertical and horizontal planes is unknown. The horizontal shift between the intersection of the beam with the surface and the actual position of the hydrometeors is called parallax shift and is 1.32 [=tan(53°)] times the altitude of the hydrometeors (Fig. 1). Bauer et al. (1998) have assessed the effect of the scanning geometry, with a particular focus on the parallax shift, on the brightness temperatures observed by two

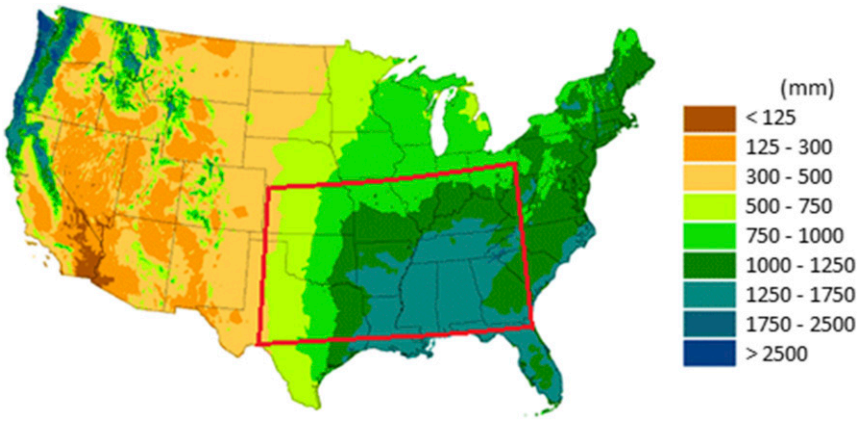

FIG. 2. Map of the continental United States with the study area (red polygon). Background color indicates the mean annual precipitation from 1961 to 2009 (credit: NOAA).

conical-scan microwave imagers (SSM/I and TMI, also having a 53° Earth incident angle) at 37 and 85 GHz for a simulated case of organized convection over the ocean. They used two radiative transfer models to simulate SSM/I and TMI TBs with various observation azimuth angles and assessed the apparent displacement of the TB patterns. They found the parallax shift to be negligible (compared to the dimensions of the footprint) at 37 GHz but significant (more than 10 km) at 85 GHz. Other studies have proposed systematic correction of the parallax shift for conical-scan microwave imagers in low Earth orbit, either assuming a constant shift (Gopalan et al. 2010) or assuming that all microwave channels are responding to the hydrometeors at the top of the clouds and exploiting the fact that cloud-top height can be accurately estimated from infrared imagery (Xu et al. 2015).

Because the 89-GHz channels of GMI are mostly sensitive to frozen hydrometeors (as the 85-GHz channels of SSM/I and TMI), the 89V TB is likely to respond to the presence of hydrometeors at high altitude in the atmosphere. For this reason, in this study, instead of comparing observed TBs to near-surface reflectivity, KuPR reflectivity is mapped relatively to the 0°C isotherm along each GMI beam [i.e., at a 53° incident angle (along the AB line in Fig. 1)] between −2000 and +16 000 m of altitude (altitude 0 m being the 0°C isotherm) through a nearest neighbor interpolation. Thus, each GMI 89V TB is associated with a KuPR reflectivity profile. A total of more than 4.7 million individual GMI 89-GHz vertically polarized TBs corresponding to 1875 GPM passes over the southeastern United States (31°–40°N, 83°–102°W) are collocated with as many KuPR along-beam and vertical reflectivity profiles between May and October from 2014 to 2017. The study area is shown in Fig. 2. It is to be noted that only the beams in the central part of GMI's swath that overlap with the KuPR swath can be collocated with reflectivity profiles. To allow for easier interpretation of the results, regions with surface elevation above 750 m, water bodies, and snow-covered areas are excluded from the analysis. Cases for which the 0°C isotherm is less than 2000 m above the surface are also excluded.

Collocated reflectivity profiles and brightness temperatures are separated into 36 classes based on the value of the observed GMI 89V TB. The first class collects all profiles with corresponding TBs being lower than 120 K; 34 classes collect the profiles with TBs ranging from 120 to 290 K (every 5 K); and the last class gathers the profiles with TBs above 290 K. Figure 3a shows the statistical distribution of the observed 89V TBs across all classes.

As stated before, over land, variations of the surface emissivity affect the observed microwave TBs. While being less variable than at lower frequencies, the surface emissivity at 89 GHz still depends on soil moisture, surface type, and surface temperature. Several methods have been proposed to mitigate the influence of the variations of the surface's radiometric properties. Spencer et al. (1989) proposed using the polarization-corrected temperature (normalized difference between vertically and horizontally polarized TBs), instead of the raw TBs for the dual-polarized channels. Petty and Li (2013) normalized all TBs by the skin temperature from ERA-Interim. More recently, You et al. (2017) proposed using the difference between the observed TB and the TB from the closest previous precipitation-free observation at the same location. Figure 3c shows that in nonprecipitating areas, variations of the ERA-Interim T_{2m} (regarded here as a proxy of the surface temperature) explain more than 80% of the 89V TB variance. To correct the 89V TB for the variations of the surface temperature, and thus retain only the precipitation-related

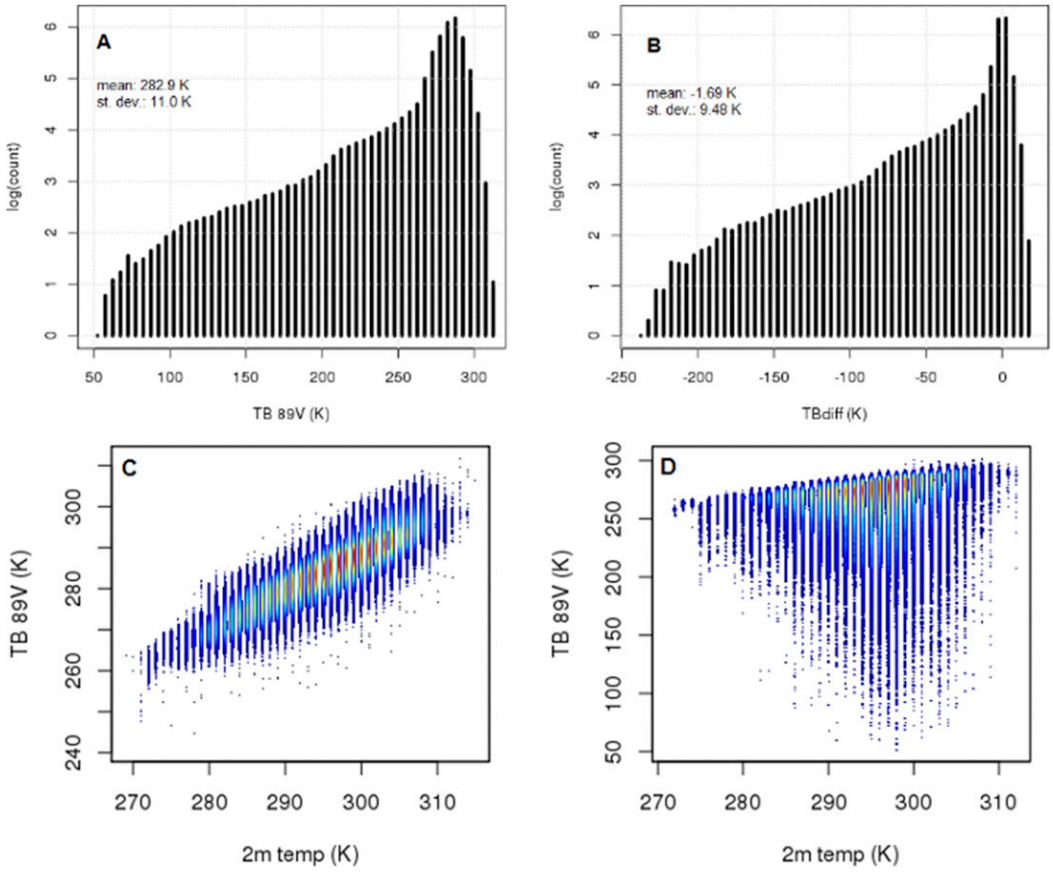

FIG. 3. (a) Statistical distribution of the 4.7 million TBs (89V TB) observed by GMI over the southeastern United States during May–October 2014–17. Vertical scale is logarithmic (decimal logarithm). Each horizontal bin is 5 K wide. (b) Statistical distribution of TB_{diff} [see Eqs. (1) and (2) for the definition of TB_{diff}]. (c) Joint distribution of TB and 2-m temperature for nonprecipitating profiles; linear correlation is 0.90. (d) Joint distribution of TB and 2-m temperature for precipitating profiles; linear correlation is 0.12. For all panels, regions with surface elevation above 750 m, water bodies, snow-covered areas, and areas where the 0°C isotherm is less than 2000 m above the surface are excluded.

TB signal, we define TB_0 as the nonprecipitating 89V TB estimated from T_{2m},

$$TB_0 = 1.00 \times T_{2m} - 10.1, \quad (1)$$

with this equation obtained by linear regression fitting the 89V TB against T_{2m} in nonprecipitating areas (Fig. 3c). We then define TB_{diff} as the difference between the GMI-observed TB and TB_0,

$$TB_{diff} = TB - TB_0, \quad (2)$$

where TB is the GMI-observed 89V TB. The statistical distribution of TB_{diff} is displayed in Fig. 3b. TB_{diff} is used as an alternative variable to tb to classify the KuPR reflectivity profiles, with one class for $TB_{diff} < -150$ K, 30 classes for TB_{diff} between −150 and 0 K (every 5 K), and one class for $TB_{diff} > 0$ K.

b. *Along-beam reflectivity profiles as function of the observed 89V TB*

The average radar reflectivity profiles along GMI's 89-GHz beam, computed for each class of TB (and for each class of TB_{diff}), are displayed in Fig. 4. As expected from the 89-GHz radiative transfer physics, lower TBs are associated with higher radar reflectivity above the 0°C isotherm (i.e., higher density and/or larger size of frozen hydrometeors) and higher echo tops (i.e., larger vertical development of cloud systems). At 89 GHz, in the studied region, during the warm season, the scattering signal from the frozen hydrometeors completely dominates the emission signal from the liquid hydrometeors. Thus, because the presence of ice hydrometeors above the 0°C isotherm is generally associated with the presence of liquid hydrometeors below the melting layer, lower TBs are also associated with higher radar reflectivity below the 0°C isotherm.

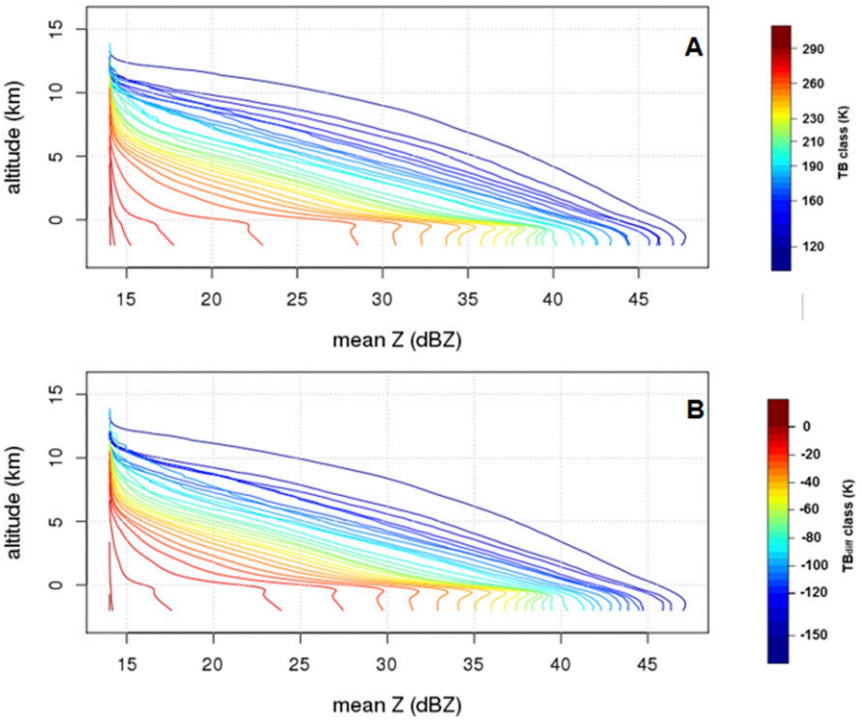

FIG. 4. (a) Mean along-beam KuPR reflectivity profile for various classes of 89V TB. (b) Mean along-beam KuPR reflectivity profile for various classes of TB_{diff}. Vertical axis is the altitude relative to the 0°C isotherm. Adjacent classes with less than 400 observed profiles are merged for the computation of the average reflectivity profile. Color scale is chosen such that the classes corresponding to the same quantiles of the distributions of TB and TB_{diff} have the same color in (a) and (b).

One can note that when using TB_{diff} instead of the raw 89V TB for the classification, the mean reflectivity profiles are nearly identical (comparing the classes corresponding to the same quantiles of the distributions of TB and TB_{diff}). The only notable differences concern the classes of TB between 270 and 285 K, and the classes of TB_{diff} between −20 and −5 K, that is, low-intensity precipitation systems causing small depressions of the 89V TB. This shows that at 89 GHz, the ice scattering signal dominates the signal associated with the variations of the surface temperature (as already shown by Fig. 3d).

For the classes corresponding to an observed TB between 210 and 270 K (or a TB_{diff} between −75 and −15 K) a local maximum of reflectivity can be observed immediately below the 0°C isotherm. This bright band, caused by the high reflectivity of melting hydrometeors, is characteristic of the stratiform precipitation regime. For classes of TB lower than 210 K (or TB_{diff} lower than −75 K), the bright band is not apparent in the average profiles. This range of TBs is then expected to characterize convective precipitation systems.

Figure 5 shows a more detailed analysis of the statistical distribution of the reflectivity profiles along GMI's beam for three classes of TB_{diff}: −15 to −10, −45 to −40, and −110 to −105 K. For each class, the mean and median profiles are shown along with the 10%, 25%, 75%, and 90% quantiles. For the −15- to −10-K class, the dispersion of the reflectivity profiles is high at all altitudes. For more than 50% of the observed profiles in this class, the echo top is found around or below the freezing level; but, it is also found higher than 2.5 km above the freezing level for 25% of the profiles, and even higher than 4 km above the freezing level for 10% of the profiles. For more than 25% of the profiles in the class, no echo is measured at any altitude. While at 2 km below the freezing level, 50% of the profiles are nonprecipitating or associated with low precipitation rates (reflectivity lower than 17 dBZ, that is, a rain rate lower than 1 mm h^{-1}) and 10% of the profiles show a reflectivity higher than 27 dBZ, corresponding to medium precipitation rates (3–8 mm h^{-1}).

For the −45- to −40-K class, the mean reflectivity, as well as the median and the 25%, 75%, and 90% quantiles, show a maximum (marking the bright band) at 500 m below the 0°C isotherm. In contrast, the 10% quantile shows a maximum at around 1500 above the 0°C isotherm. The measured reflectivities are therefore

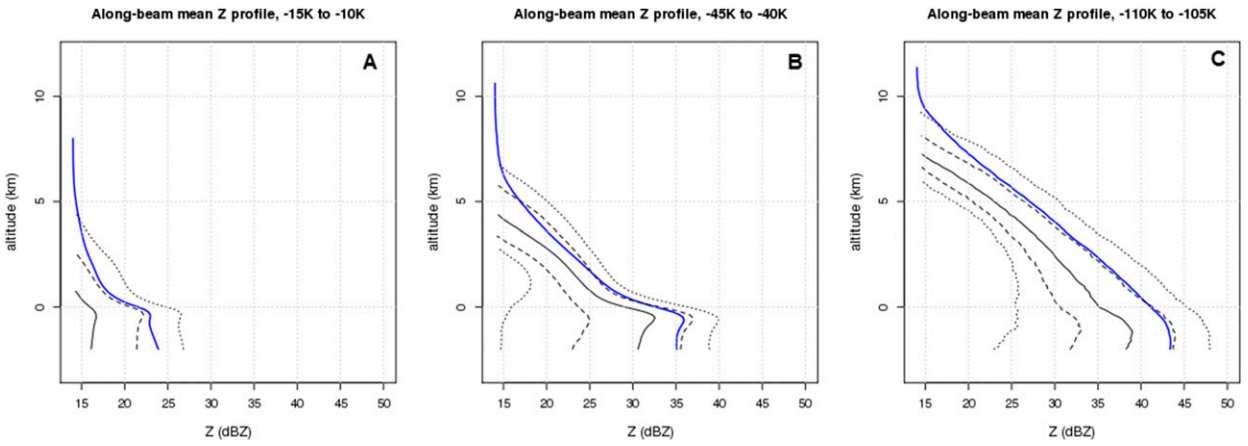

FIG. 5. Mean KuPR reflectivity profile (thick blue line), for three different classes of TB_{diff}: (a) −15 to −10, (b) −45 to −40, and (c) −110 to −105 K. The statistical dispersion of the reflectivity in each class and for each altitude level is represented by the 25% and 75% quantiles (dashed lines) and the 10% and 90% quantiles (dotted lines). The thick black line shows the median of the distribution at each altitude level. The vertical axis is the altitude relative to the 0°C isotherm. The 10% and 25% quantiles do not appear in (a) because their value is zero ($-\infty$ in dBZ units) at every altitude level.

much more spread below the freezing level than above: at 1500 m above the freezing level, the 80% confidence interval ranges from 18 to 27 dBZ; at 2000 m below the freezing level, the 80% confidence interval ranges from 14.5 to 39.5 dBZ. For 90% of the profiles in this class, the echo top is found at least 3 km above the freezing level and is therefore expected to almost exclusively relate to hydrometeors in the solid phase. Except for the absence of the bright band, the −110- to −105-K class shows similar characteristics with the −45- to −40-K class. The 10%–90% interquantile is much larger below the freezing level than above. For 90% of the observations, the echo tops are found more than 6 km above the 0°C isotherm. Consequently, a more than 105-K depression of the TB 89V quasi certainly indicates the presence of frozen hydrometeors in the upper troposphere, characteristic of deep convection. Nevertheless, a value of TB_{diff} lower than 105 K does not necessarily indicate heavy precipitation rates at near-surface levels as implied by the very wide range of the observed reflectivities below the 0°C isotherm: the 80% confidence interval 2 km below the freezing level ranges from 22.5 to 48 dBZ for the −105- to −110-K class.

The analysis of the reflectivity profiles conditioned on the value of TB (or TB_{diff}) shows that a low 89V TB is a clear indicator of the presence of frozen hydrometeors above the 0°C isotherm. This is consistent with the well-known physics of the 89-GHz radiative transfer in the atmosphere: the scattering of microwaves by ice particles leads to depression in observed TBs (Ulaby et al. 1981; Spencer et al. 1989). While the radar reflectivity above the freezing level along GMI's 89-GHz beam is relatively well constrained by the value of TB_{diff} when TB_{diff} is lower than −40 K, the statistical dispersion of the observed reflectivities is high below the freezing level for every class. The fact that the radar reflectivity above the freezing level does not always correlate well with the radar reflectivity below the freezing level can be partially explained by the reflectivity profiles being mapped along GMI's 89-GHz beam with a 53° Earth incident angle instead of vertical profiles. Therefore, a high Earth incident angle may be considered as a limitation, from the perspective of the retrieval of surface precipitation from conical-scan passive microwave imagers, particularly for resolving the fine-scale patterns in cases with strong local heterogeneity.

We assume here that the dispersion of observed KuPR reflectivities for a given TB class reflects the physical variability of the observed systems rather than KuPR retrieval errors. This seems reasonable considering the magnitude of the found dispersion compared to the accuracy of the KuPR (evaluated by Chen and Chandrasekar 2016) and its predecessor, the Precipitation Radar on board TRMM (evaluated by Islam et al. 2012). We note that the KuPR reflectivity profiles used here are corrected for path-integrated attenuation. This necessarily imperfect correction is naturally larger for low-altitude reflectivities, which are consequently retrieved with lower accuracy, particularly for very deep systems. This is, however, likely to explain only a small portion of the very large dispersion of observed near-surface reflectivities.

c. *Altitude of hydrometeors to which the 89V TB is responding*

The main objective of the analysis is to determine the altitude level to which the 89V TB is primarily responding. Figure 6a shows the linear correlation between TB

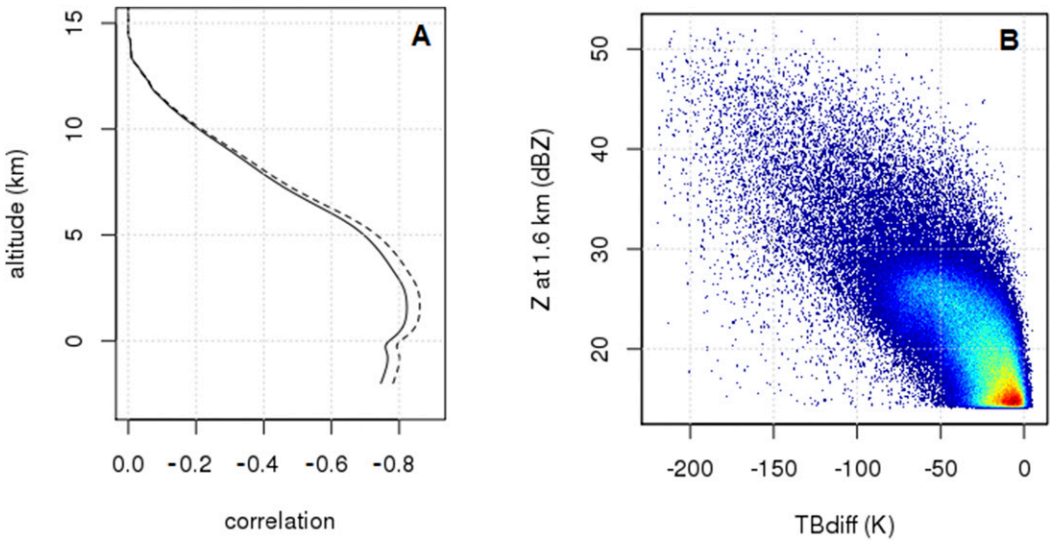

FIG. 6. (a) Linear correlation between TB and KuPR $Z(y)$ in dBZ units along GMI's 89-GHz beam as a function of y (relative to the 0°C isotherm; thick line). Linear correlation between TB_{diff} and $Z(y)$ as a function of the altitude y (dashed line). Only profiles with TB < 285 K (and $TB_{diff} < 0$ K) are retained for the computation of the correlations. (b) Scatterplot of KuPR reflectivity Z at 1.6 km above the 0°C isotherm against TB_{diff}.

in the 50–285-K range (TB_{diff} from -250 to 0 K) and the radar reflectivity $Z(y)$ in dBZ units inside GMI's 89-GHz beam, as a function of altitude y. It appears that TB (TB_{diff}) is strongly anticorrelated to reflectivity between 300 m and 4 km above the 0°C isotherm with a -0.82 (-0.86) minimum correlation coefficient 1.6 km above the 0°C isotherm. The anticorrelation of TB and TB_{diff} with reflectivity below the freezing level is significantly weaker. Figure 6b shows the joint distribution of TB_{diff} and reflectivity 1.6 km above the 0°C isotherm as a scatterplot. If the 89V TB seems to be responding primarily to the hydrometeors 1.6 km above the 0°C isotherm, this optimal value arises only as an average over a wide range of precipitation systems with different characteristics. Actually, as colder TBs are associated with precipitation systems with larger vertical development, they likely correlate with reflectivity of frozen hydrometeors at a higher altitude. Similar to Fig. 6a, Fig. 7a shows the correlation between TB (TB_{diff}) and reflectivity at various altitude levels, but only for TBs in the 50–160-K range (TB_{diff} from -250 to -125 K). Reducing the analysis to the very cold TBs (specifically the 0.1% lower percentile of the distributions of TB and TB_{diff}), we find maximum anticorrelations 7 km above the freezing level, which confirms the previous assumption. One can note that in this range of TB and TB_{diff}, the anticorrelation with reflectivities around and below the 0°C isotherm is very low. This confirms that for deep convective systems, along GMI's 89-GHz beam, the intensity of the convection does not necessarily correlate with the intensity of surface precipitation. While, as stated before, this may be partially related to the high incidence angle of GMI, it is also consistent with the findings of Hamada et al. (2014, p. 8166) from the analysis of 12 years of TRMM Precipitation Radar data (vertical profiles) focused on extreme precipitation, which conclude that "the higher convective intensity does not necessarily correspond to the higher rainfall rates, especially over land."

To obtain a statistical relation between TB_{diff} and the altitude of the hydrometeors to which it is responding, we searched for the altitude of the maximum anticorrelation with the radar reflectivity for various ranges of TB_{diff}. Each range is initially defined as a 2-K interval. The interval is then widened until the maximum anticorrelation reaches a significant level. Figure 7b shows the altitude of the maximum anticorrelation for various ranges of TB_{diff}. One can see that in the range of TB_{diff} higher than -15 K, the maximum anticorrelation is consistently found 300 m below the freezing level. For TB_{diff} lower than -15 K, the altitude of the maximum anticorrelation increases with decreasing TB_{diff}.

d. *Correction of the parallax shift*

Bauer et al. (1998) defined the center of gravity of the spectral weighting function for a given channel as the expected value of the $C(y)$ distribution; $C(y)$ represents the normalized contribution of the atmospheric layer of y to the observed TB. They found that at 85 GHz, in convective areas, the $C(y)$ distribution is symmetrical with a maximum close to its expected value. It appears

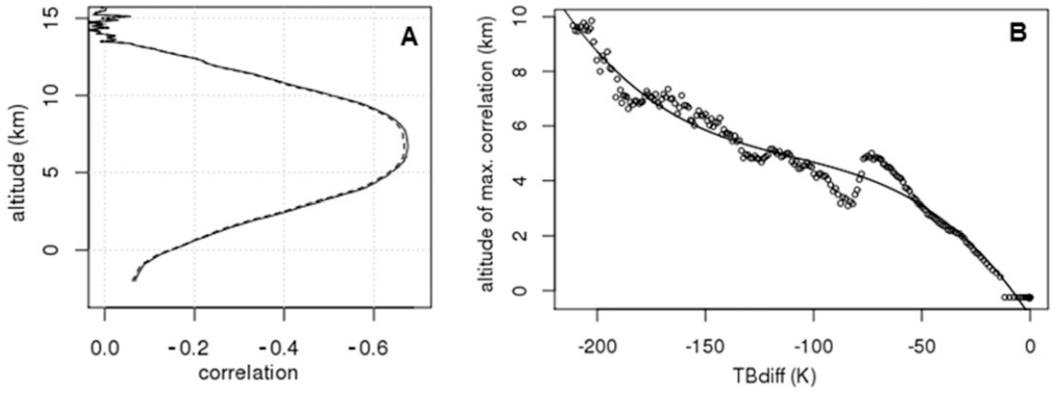

FIG. 7. (a) Linear correlation between TB and the KuPR reflectivity $Z(y)$ in dBZ units along GMI's 89-GHz beam as a function of the altitude y (relative to the 0°C isotherm) for TB between 50 and 160 K (0.1% lower percentile; thick line). Linear correlation between TB_{diff} and $Z(y)$ as function of the altitude y for TB_{diff} between −250 and −125 K (0.1% lower percentile; dashed line). (b) The dots show altitude (relative to the 0°C isotherm) of the maximum anticorrelation of TB_{diff} with $Z(y)$ for various ranges of TB_{diff}. The abscissa position of each dot corresponds to the mean value of TB_{diff} in each range. The black line shows the regressed third-order polynomial function used to estimate the altitude of the center of gravity of the ice and to correct the parallax shift in GMI observations at 89 GHz.

then as a reasonable assumption that the altitude at which the radar reflectivity correlates better with TB_{diff} corresponds to the center of gravity of the spectral weighting function at 89 GHz. Therefore, for each range of TB_{diff}, the altitude of the maximum anticorrelation is interpreted here as the mean altitude of the hydrometeors to which the 89V TB is responding. Using this information, we can correct the parallax shift of each individual GMI observation at 89 GHz, based on the value of TB_{diff}. For TB_{diff} lower than −5 K, we obtained the following relation between the altitude of the center of gravity and TB_{diff} using a third-order polynomial regression:

$$\gamma = -0.937 - 0.119 \times TB_{diff} - 9 \times 10^{-4} \times TB_{diff}^2 - 3 \times 10^{-4} \times TB_{diff}^3, \quad (3)$$

with γ as the altitude of the center of gravity relative to the 0°C isotherm (km). If TB_{diff} is higher than −5 K, we assume that it is constantly responding to the −300-m altitude level. Using this relation, we can assess the location of the center of gravity of the ice clusters causing the depressions in the observed 89V TBs in both the vertical and horizontal planes. It is expected that the observed 89V TB is more closely related to the surface precipitation directly below the ice clusters than to the surface precipitation at the intersection of the GMI's beam with the surface. As illustrated in Fig. 1, point B corresponds to the center of gravity of the ice inside the 89-GHz beam; TB (or TB_{diff}) is expected to correlate better with the precipitation rate at point C (vertical projection of point B on the surface) than with the precipitation rate at point A (intersection of the beam with the surface).

For each individual GMI beam, the positions of points B and C are determined using Eq. (3). Figure 8 (left) shows the relation between TB_{diff} and the radar-derived surface precipitation rate without parallax correction (i.e., precipitation rate at point A) as a scatterplot. The right panel shows the scatterplot of the surface precipitation rate against TB_{diff} with parallax correction (i.e., precipitation rate at point C). One can see that with the parallax correction, values of TB_{diff} lower than −60 K are systematically associated with above-zero near-surface precipitation rates, while about 4% of TB_{diff} values lower than −60 K are associated with nonprecipitating radar observations when the parallax is ignored. A second-order polynomial regression of the surface precipitation rate against TB_{diff} is performed for both cases (dashed lines in Fig. 8). The regression residual variance is 1.76 $mm^2 h^{-2}$ without parallax correction and 1.42 $mm^2 h^{-2}$ with parallax correction. As expected, the parallax correction mostly improves the relation between TB and surface precipitation for the cold TBs, corresponding to the intense convective precipitation systems. The two regressed polynomial functions diverge in the range of TB_{diff} lower than −50 K, the function regressed with the parallax correction being significantly higher.

4. Discussion and conclusions

The results shown here shed light on the challenges regarding the retrieval of the finescale spatial patterns (typically scales finer than 40 km) of instantaneous

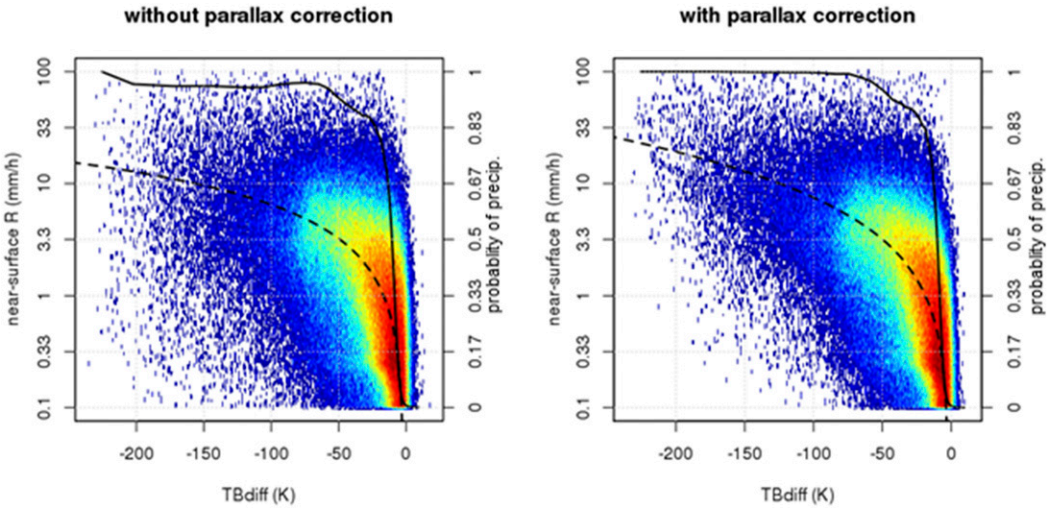

FIG. 8. (left) Scatterplot of KuPR precipitation rate at point A (Fig. 1) against TB_{diff}. (right) Scatterplot of KuPR precipitation rate at point C (Fig. 1) against TB_{diff}. The position of point C is determined using Eq. (3). In both panels, the thick lines show the probability of an above-zero radar precipitation rate as a function of the observed TB_{diff} (see right vertical axis for the scale). The dashed lines are the second-order polynomial functions regressed onto precipitation rates against TB_{diff}.

surface precipitation over land from passive microwave sensors. In GMI's case, information from the 89-GHz channels is easier to exploit because, contrary to lower-frequency channels, the 89-GHz TBs are mildly affected by variations of surface emissivity. The fact that the TB at 89 GHz is primarily affected by ice scattering occurring in the upper layers of cloud systems (above the freezing level) is well known. Although the ice scattering signal is dominant at 89 GHz in the studied region, the marginal variability caused by changes in the surface temperature is handled here using estimates of the temperature at 2 m from ERA-Interim. TB_{diff} is defined as the 89-GHz vertically polarized TB corrected for the variations of the surface temperature [Eq. (2)]. While snow-covered surfaces, known to have a very low emissivity at 89 GHz, are excluded from the analysis, variations of surface type, vegetation, and soil moisture are ignored. Using the southeastern part of the continental United States as a test bed, our study confirms that 89V TB is mostly sensitive to the presence of frozen hydrometeors up to 10 km above the 0°C isotherm. Moreover, it provides a quantitative assessment of the statistical relations between ice's radar reflectivity, vertical development of the systems, and observed brightness temperature. It is shown that the radar reflectivity of ice hydrometeors 1.6 km above the freezing level can be relatively well predicted from the measured TB (with a −0.86 linear correlation between TB_{diff} and Z).

Passive microwave precipitation retrieval algorithms are generally designed to estimate the precipitation rate close to the intersection of the radiometer field of view with Earth's surface. As the 89V TB is a good indicator of the presence of ice in the upper troposphere, and because convective systems over land are typically characterized by ice-phase hydrometeors at high altitudes (Nesbitt et al. 2000; Luo et al. 2008; Houze et al. 2015), one may assume that surface precipitation shall be well retrieved from passive microwave algorithms for the convective cases. Nevertheless, the present study reveals that even if a very low value of TB_{diff} is a reliable indicator of deep convection, it is not always associated with intense near-surface precipitation inside the field of view of the imager. This is partially explained by the high incidence angle of GMI, because the high-altitude ice clusters generating depressions of the 89-GHz TB are horizontally shifted relatively to the surface field of view (see Fig. 1). As this parallax shift is typically 9–16 km, it appears necessary to account for it to resolve precipitation patterns at scales finer than 40 km. The parallax shift can be corrected only if the altitude of the hydrometeors to which the TB is responding is known. In the present study, an empirical relation between TB_{diff} and the altitude of the center of gravity of the ice hydrometeors relative to the freezing level is derived over the southeastern continental United States during the warm season. With the parallax correction, TB_{diff} appears more closely related to the surface precipitation rate. The improvement is more salient for very low values of TB_{diff}, corresponding to the most intense precipitation rates. Taking the parallax shift into account shall therefore efficiently improve the retrieval of the extreme convective precipitation systems over land. However, it is uncertain whether the relation between the observed

89V TB and the altitude of the center of gravity of the ice hydrometers derived regionally is valid globally over land surfaces. Future work will focus on establishing a more general and more flexible way to systematically account for the parallax in the retrieval.

Even with the parallax correction, TB_{diff} remains a modest predictor of the surface precipitation rate because of the tenuous relation between ice reflectivity above the melting layer and instantaneous surface precipitation. Among the elements that may explain this fact is the delay induced by the fall time of the hydrometeors. For deep convective systems, considering the fall velocity of solid hydrometeors (Fabry and Zawadzki 1995), the hydrometeors located between 3 and 10 km above the melting layer may take more than 15 min to reach the melting layer and ultimately the surface, while GMI and KuPR collocated instantaneous measurements are less than a minute apart. More generally, decorrelation between high-altitude radar reflectivity and near-surface reflectivity is a consequence of the vertical heterogeneity of precipitation systems (Leary and Houze 1979; Rosenfeld and Mintz 1988). This heterogeneity is naturally more pronounced at short time scales for highly dynamic systems with strong vertical development. A higher altitude of the 0°C isotherm is also prone to weaken the relation between solid-phase hydrometeors' sizes and the density above the freezing level and the instantaneous surface rain rate. Consequently, in spite of the strong ice signature at 89 GHz, the finescale patterns of instantaneous surface precipitation over land are not necessarily better retrieved for the deepest convective systems. In Guilloteau et al. (2017), the best retrieval of the finescale patterns of surface precipitation over land from GMI with the GPROF algorithm (not accounting for the parallax) was seen over Europe and Siberia, where convection is less deep and the bright band is less elevated compared to lower latitudes.

The 89-GHz channels of GMI have a smaller footprint at the surface than any of the lower-frequency channels (the 10.6-GHz footprint is 19 km × 32 km, while the 89-GHz footprint is 4.4 km × 7.1 km). Nevertheless, the findings of this study explain the limited ability of the ice-scattering-sensitive channels to resolve the finescale patterns of surface precipitation. Guilloteau et al. (2017) found that GMI can resolve precipitation at finer scales over oceans (down to 20 or 10 km) by relying on the rain's emission signal at frequencies between 10 and 40 GHz. This emphasizes the need to improve the exploitation of the information from low-frequency channels over land, as these are directly affected by liquid hydrometeors at lower altitudes. This may be achieved by including a priori information on surface emissivity (Ferraro et al. 2013; Turk et al. 2016), or by combining the various channels so they become insensitive to variations of ground emissivity (Petty and Li 2013).

Acknowledgments. This work was supported by the NASA Global Precipitation Measurement Program under Grant NNX16AO56G. The authors thank editor Prof. Tristan L'Ecuyer and the three reviewers for their insightful comments, which helped to improve the methodology and the presentation of the results.

APPENDIX

Acronyms

AMSR-2	Advanced Microwave Scanning Radiometer 2
DMSP	Defense Meteorological Satellite Program
DPR	Dual-Frequency Precipitation Radar
ECMWF	European Centre for Medium-Range Weather Forecasts
ERA	ECMWF Re-Analysis
GCOM-W1	*Global Change Observation Mission–Water*
GANAL	Japan Meteorological Agency Global Analysis
GMI	GPM Microwave Imager
GPM	Global Precipitation Measurement
GPROF	Goddard profiling algorithm
GSMaP	Global Satellite Mapping of Precipitation
H 01-CDRD	H SAF Cloud Dynamics and Radiation Database, product 01
H SAF	EUMETSAT Satellite Application Facility on Support to Operational Hydrology and Water Management
JAXA	Japan Aerospace Exploration Agency
KuPR	Ku precipitation radar
NASA	National Aeronautics and Space Administration
SSM/I	Special Sensor Microwave Imager
SSM/IS	Special Sensor Microwave Imager/Sounder
TB	Brightness temperature
TMI	TRMM Microwave Imager
TRMM	Tropical Rainfall Measuring Mission

REFERENCES

Aonashi, K., and Coauthors, 2009: GSMaP passive microwave precipitation retrieval algorithm: Algorithm description and validation. *J. Meteor. Soc. Japan*, **87A**, 119–136, https://doi.org/10.2151/jmsj.87A.119.

Awaka, J., M. Le, V. Chandrasekar, N. Yoshida, T. Higashiuwatoko, T. Kubota, and T. Iguchi, 2016: Rain type classification algorithm module for GPM dual-frequency precipitation radar. *J. Atmos. Oceanic Technol.*, **33**, 1887–1898, https://doi.org/10.1175/JTECH-D-16-0016.1.

Bauer, P., L. Schanz, and L. Roberti, 1998: Correction of three-dimensional effects for passive microwave remote sensing of

convective clouds. *J. Appl. Meteor.*, **37**, 1619–1632, https://doi.org/10.1175/1520-0450(1998)037<1619:COTDEF>2.0.CO;2.

Chen, H., and V. Chandrasekar, 2016: Validation of NASA's Global Precipitation Measurement mission with a high-resolution ground radar network. *Proc. 2016 URSI Asia–Pacific Radio Science Conf. (URSI AP-RASC 2016)*, Seoul, South Korea, IEEE, 836–839, https://doi.org/10.1109/URSIAP-RASC.2016.7601343.

Draper, D. W., D. A. Newell, F. J. Wentz, S. Krimchansky, and G. M. Skofronick-Jackson, 2015: The Global Precipitation Measurement (GPM) microwave imager (GMI): Instrument overview and early on-orbit performance. *IEEE J. Sel. Top. Appl. Earth Obs. Remote Sens.*, **8**, 3452–3462, https://doi.org/10.1109/JSTARS.2015.2403303.

Ebtehaj, A. M., R. L. Bras, and E. Foufoula-Georgiou, 2015: Shrunken locally linear embedding for passive microwave retrieval of precipitation. *IEEE Trans. Geosci. Remote Sens.*, **53**, 3720–3736, https://doi.org/10.1109/TGRS.2014.2382436.

Fabry, F., and I. Zawadzki, 1995: Long-term radar observations of the melting layer of precipitation and their interpretation. *J. Atmos. Sci.*, **52**, 838–851, https://doi.org/10.1175/1520-0469(1995)052<0838:LTROOT>2.0.CO;2.

Ferraro, R. R., and Coauthors, 2013: An evaluation of microwave land surface emissivities over the continental United States to benefit GPM-era precipitation algorithms. *IEEE Trans. Geosci. Remote Sens.*, **51**, 378–398, https://doi.org/10.1109/TGRS.2012.2199121.

Gopalan, K., N.-Y. Wang, R. Ferraro, and C. Liu, 2010: Status of the TRMM 2A12 land precipitation algorithm. *J. Atmos. Oceanic Technol.*, **27**, 1343–1354, https://doi.org/10.1175/2010JTECHA1454.1.

GPM Science Team, 2016a: GPM GMI common calibrated brightness temperatures collocated L1C 1.5 hours 13 km, V05. Goddard Earth Sciences Data and Information Services Center, accessed 16 February 2018, https://doi.org/10.5067/GPM/GMI/GPM/1C/05.

——, 2016b: GPM DPR Ku precipitation profile 2A 1.5 hours 5 km, V05. Goddard Earth Sciences Data and Information Services Center, accessed 16 February 2018, https://doi.org/10.5067/GPM/DPR/KU/2A/05.

Grecu, M., W. S. Olson, S. J. Munchak, S. Ringerud, L. Liao, Z. Haddad, B. L. Kelley, and S. F. McLaughlin, 2016: The GPM combined algorithm. *J. Atmos. Oceanic Technol.*, **33**, 2225–2245, https://doi.org/10.1175/JTECH-D-16-0019.1.

Guilloteau, C., E. Foufoula-Georgiou, and C. D. Kummerow, 2017: Global multiscale evaluation of satellite passive microwave retrieval of precipitation during the TRMM and GPM eras: Effective resolution and regional diagnostics for future algorithm development. *J. Hydrometeor.*, **18**, 3051–3070, https://doi.org/10.1175/JHM-D-17-0087.1.

Hamada, A., Y. Murayama, and Y. N. Takayabu, 2014: Regional characteristics of extreme rainfall extracted from TRMM PR measurements. *J. Climate*, **27**, 8151–8169, https://doi.org/10.1175/JCLI-D-14-00107.1.

Hou, A. Y., and Coauthors, 2014: The Global Precipitation Measurement mission. *Bull. Amer. Meteor. Soc.*, **95**, 701–722, https://doi.org/10.1175/BAMS-D-13-00164.1.

Houze, R. A., K. L. Rasmussen, M. D. Zuluaga, and S. R. Brodzik, 2015: The variable nature of convection in the tropics and subtropics: A legacy of 16 years of the Tropical Rainfall Measuring Mission satellite. *Rev. Geophys.*, **53**, 994–1021, https://doi.org/10.1002/2015RG000488.

Islam, T., M. A. Rico-Ramirez, D. Han, P. K. Srivastava, and A. M. Ishak, 2012: Performance evaluation of the TRMM precipitation estimation using ground-based radars from the GPM validation network. *J. Atmos. Sol.-Terr. Phys.*, **77**, 194–208, https://doi.org/10.1016/j.jastp.2012.01.001.

Kummerow, C. D., W. Barnes, T. Kozu, J. Shiue, and J. Simpson, 1998: The Tropical Rainfall Measuring Mission (TRMM) sensor package. *J. Atmos. Oceanic Technol.*, **15**, 809–817, https://doi.org/10.1175/1520-0426(1998)015<0809:TTRMMT>2.0.CO;2.

——, J. Simpson, O. Thiele, W. Barnes, A. T. C. Chang, E. Stocker, and P. Ashcroft, 2000: The status of the Tropical Rainfall Measuring Mission (TRMM) after two years in orbit. *J. Appl. Meteor.*, **39**, 1965–1982, https://doi.org/10.1175/1520-0450(2001)040<1965:TSOTTR>2.0.CO;2.

——, and Coauthors, 2001: The evolution of the Goddard Profiling Algorithm (GPROF) for rainfall estimation from passive microwave sensors. *J. Appl. Meteor.*, **40**, 1801–1820, https://doi.org/10.1175/1520-0450(2001)040<1801:TEOTGP>2.0.CO;2.

——, D. L. Randel, M. Kulie, N. Y. Wang, R. Ferraro, J. S. Munchak, and V. Petković, 2015: The evolution of the Goddard profiling algorithm to a fully parametric scheme. *J. Atmos. Oceanic Technol.*, **32**, 2265–2280, https://doi.org/10.1175/JTECH-D-15-0039.1.

Leary, C. A., and R. A. Houze, Jr., 1979: Melting and evaporation of hydrometeors in precipitation from the anvil clouds of deep tropical convection. *J. Atmos. Sci.*, **36**, 669–679, https://doi.org/10.1175/1520-0469(1979)036<0669:MAEOHI>2.0.CO;2.

Liu, J., C. D. Kummerow, and G. S. Elsaesser, 2017: Identifying and analysing uncertainty structures in the TRMM microwave imager precipitation product over tropical ocean basins. *Int. J. Remote Sens.*, **38**, 23–42, https://doi.org/10.1080/01431161.2016.1259676.

Luo, Z., G. Y. Liu, and G. L. Stephens, 2008: CloudSat adding new insight into tropical penetrating convection. *Geophys. Res. Lett.*, **35**, L19819, https://doi.org/10.1029/2008GL035330.

Mugnai, A., and Coauthors, 2013: CDRD and PNPR satellite passive microwave precipitation retrieval algorithms: EuroTRMM/EURAINSAT origins and H-SAF operations. *Nat. Hazards Earth Syst. Sci.*, **13**, 887, https://doi.org/10.5194/nhess-13-887-2013.

Nesbitt, S. W., E. J. Zipser, and D. J. Cecil, 2000: A census of precipitation features in the tropics using TRMM: Radar, ice scattering, and lightning observations. *J. Climate*, **13**, 4087–4106, https://doi.org/10.1175/1520-0442(2000)013<4087:ACOPFI>2.0.CO;2.

Oliveira, R. A., R. C. Braga, D. Vila, and C. A. Morales, 2015: Evaluation of GPROF-SSMI/S rainfall estimates over land during the Brazilian CHUVA-VALE campaign. *Atmos. Res.*, **163**, 102–116, https://doi.org/10.1016/j.atmosres.2014.11.010.

Petković, V., and C. D. Kummerow, 2017: Understanding the sources of satellite passive microwave rainfall retrieval systematic errors over land. *J. Appl. Meteor. Climatol.*, **56**, 597–614, https://doi.org/10.1175/JAMC-D-16-0174.1.

——, ——, D. L. Randel, J. R. Pierce, and J. K. Kodros, 2018: Improving the quality of heavy precipitation estimates from satellite passive microwave rainfall retrievals. *J. Hydrometeor.*, **19**, 69–85, https://doi.org/10.1175/JHM-D-17-0069.1.

Petty, G. W., and K. Li, 2013: Improved passive microwave retrievals of rain rate over land and ocean. Part I: Algorithm description. *J. Atmos. Oceanic Technol.*, **30**, 2493–2508, https://doi.org/10.1175/JTECH-D-12-00144.1.

Rosenfeld, D., and Y. Mintz, 1988: Evaporation of rain falling from convective clouds as derived from radar Measurements. *J. Appl. Meteor.*, **27**, 209–215, https://doi.org/10.1175/1520-0450(1988)027<0209:EORFFC>2.0.CO;2.

Skofronick-Jackson, G., and Coauthors, 2016: The Global Precipitation Measurement (GPM) mission for science and society.

Bull. Amer. Meteor. Soc., **98**, 1679–1695, https://doi.org/10.1175/BAMS-D-15-00306.1.

Spencer, R. W., H. M. Goodman, and R. E. Hood, 1989: Precipitation retrieval over land and ocean with the SSM/I: Identification and characteristics of the scattering signal. *J. Atmos. Oceanic Technol.*, **6**, 254–273, https://doi.org/10.1175/1520-0426(1989)006<0254:PROLAO>2.0.CO;2.

Tang, L., Y. Tian, and X. Lin, 2014: Validation of precipitation retrievals over land from satellite-based passive microwave sensors. *J. Geophys. Res. Atmos.*, **119**, 4546–4567, https://doi.org/10.1002/2013JD020933.

Turk, F. J., Z. S. Haddad, and Y. You, 2016: Estimating nonraining surface parameters to assist GPM constellation radiometer precipitation algorithms. *J. Atmos. Oceanic Technol.*, **33**, 1333–1353, https://doi.org/10.1175/JTECH-D-15-0229.1.

Ulaby, F. T., R. K. Moore, and A. K. Fung, 1981: *Microwave Remote Sensing Fundamentals and Radiometry*. Vol. 1, *Microwave Remote Sensing: Active and Passive*, Addison-Wesley, 470 pp.

Xu, B., P. Xie, M. Xu, L. Jiang, C. Shi, and R. You, 2015: A validation of passive microwave rain-rate retrievals from the Chinese *FengYun-3B* satellite. *J. Hydrometeor.*, **16**, 1886–1905, https://doi.org/10.1175/JHM-D-14-0143.1.

You, Y., C. Peters-Lidard, J. Turk, S. Ringerud, and S. Yang, 2017: Improving overland precipitation retrieval with brightness temperature temporal variation. *J. Hydrometeor.*, **18**, 2355–2383, https://doi.org/10.1175/JHM-D-17-0050.1.